Spray-Drying-Engineered CS/HA-Bilayer Microneedles Enable Sequential Drug Release for Wound Healing

Haowen Zhong[1,2,3,4] *, Zongyou Chen*[1,2,3,4]*,Jiahao Huang*[1,2,3,4] *, Xiao Yu*[1,2,3,4] *, Chengyong Wang*[1,2,3,4]*, Yue Zheng*[5] *and Mengran Peng*[6]*, Zhishan Yuan*[1,2,3,4,*]

1. School of Electro-mechanical Engineering, Guangdong University of Technology, Guangzhou, 510006, China;
2. Guangdong Provincial Key Laboratory of Minimally Invasive Surgical Instruments and Manufacturing Technology, Guangdong University of Technology, Guangzhou, 510006, China；
3. State Key Laboratory for High Performance Tools, Guangdong University of Technology, Guangzhou, 510006, China;
4. Smart Medical Innovation Technology Center, Guangdong University of Technology, Guangzhou, 510006, China;
5. Nanfang Hospital, Southern Medical University, Guangzhou, 510006, China;
6. Department of Dermatology, the Third Affiliated Hospital of Sun Yat-sen University, Guangzhou, 510006, China;

* E-mail of corresponding author: zhishanyuan@gdut.edu.cn;

S1. Chitosan was dried and molded in different molds.

Firstly, pour the chitosan solution into the PDMS mold and the copper/PDMS mold separately, and perform vacuum pumping. Then, the mold was dried for 12 hours under the same drying conditions. Finally, use a microscope to observe at a fixed angle whether the chitosan microspheres have undergone deformation. As shown in Fig. S1, CS microneedles prepared using PDMS molds undergo significant deformation. In contrast, CS microneedles prepared using Copper/PDMS molds did not show significant deformation.

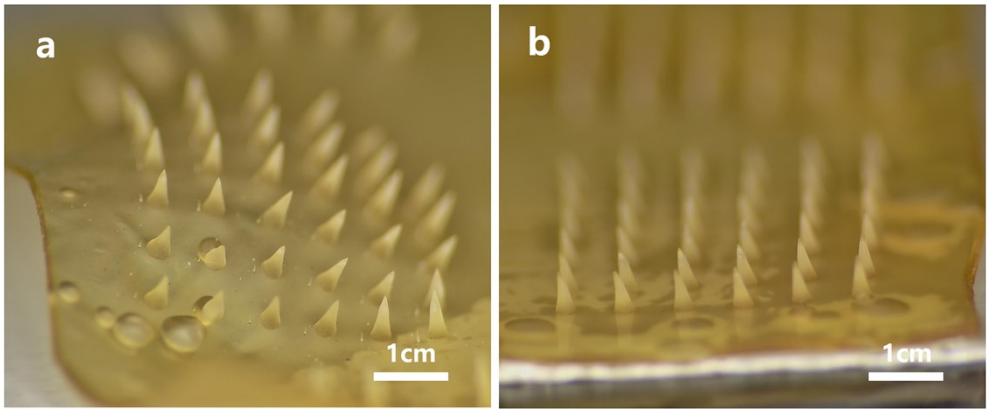

Fig. S1. (a) CS microneedles prepared using PDMS molds; (b) CS microneedles prepared using Copper/PDMS molds

S2. Physical image of automatic spraying equipment.

In this study, the laboratory independently built spraying equipment capable of controlling atomized particle size, spraying speed, and spraying timing. As shown in Fig. S2(a-b), the machine is primarily composed of a three-dimensional (3D) mobile platform, a Z-axis motorized linear stage, an airbrush, and an air pump with a time relay. The time relay regulates the output of air or liquid by controlling the opening and closing of two spray control valves and determines the duration of their operation. Samples are fixed on the 3D mobile platform, which allows for reciprocating motion, while the Z-axis motorized stage adjusts the height between the sample and the airbrush. Additionally, the airbrush enables precise adjustment of the atomized particle size. The distance between the sample and the airbrush was maintained at 15 cm, with the air pump pressure set within the range of 0.2 to 0.3 MPa. The air and liquid output durations of the spray gun were calibrated to 2 seconds and 4 seconds, respectively, with alternating cycles. The total spraying time was maintained for 10 minutes.

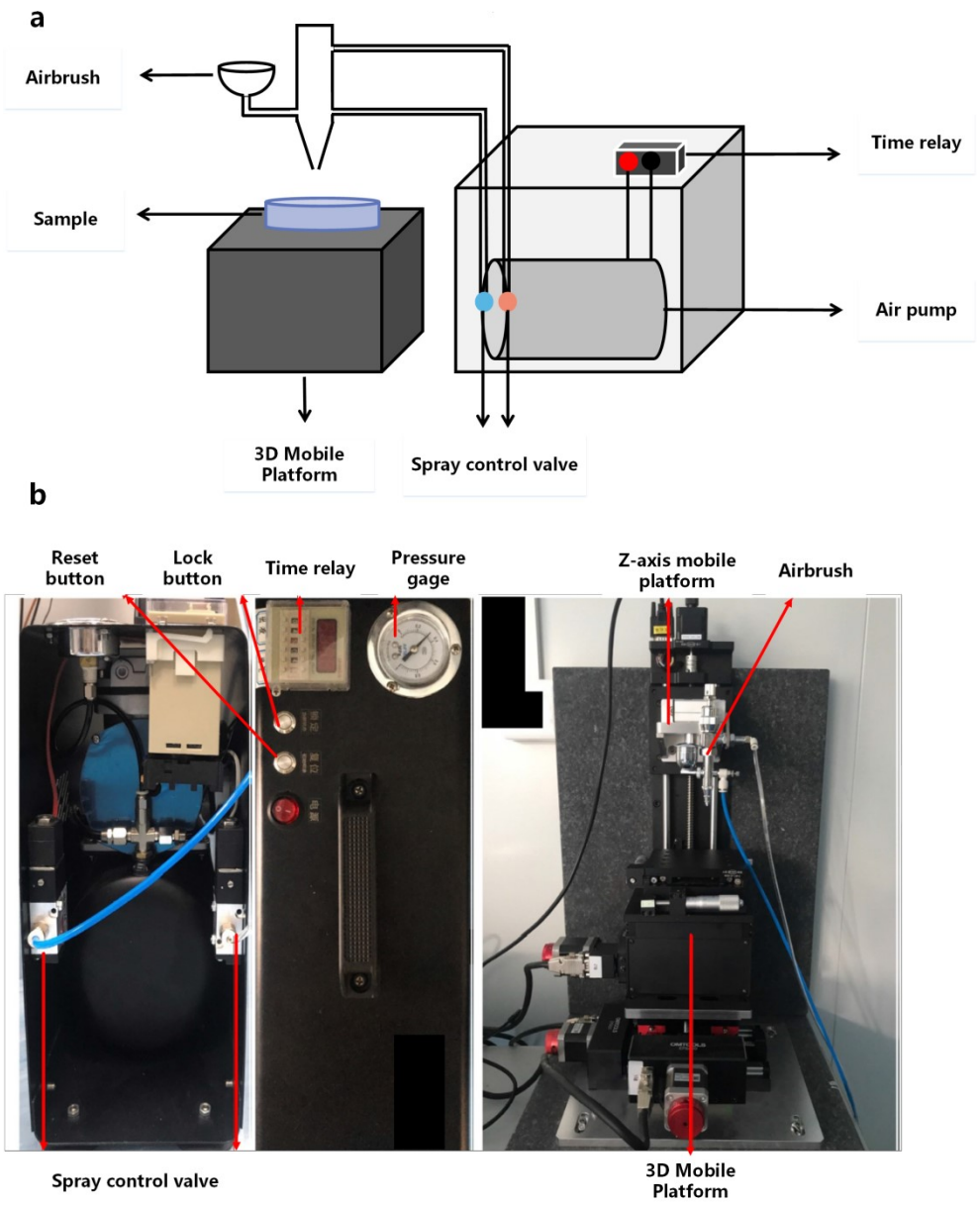

Fig. S2. (a) Schematic diagram of automatic spraying equipment. (b) Physical image of automatic spraying equipment.

S3. Physical image of Mechanical properties testing machine

In this study, the laboratory used an independently built mechanical properties testing machine to measure the axial force leading to the failure of CS/HA-bilayer MNs. A schematic diagram of the machine is presented in Fig. S3(a). The machine consists of a control panel, a linear module, a microscope system, a mobile platform, a computer, and a force sensor, as shown in Fig. S3(b). During the test, the MNs was fixed on the force sensor, and the linear module moved the force sensor at a speed of 0.3 mm/s. The force sensor recorded mechanical data at a frequency of 400 Hz and an accuracy of 0.01 N, transmitting the data to a computer for further analysis. Meanwhile, the microscope continuously recorded and stored the deformation of the MNs during the compression process.

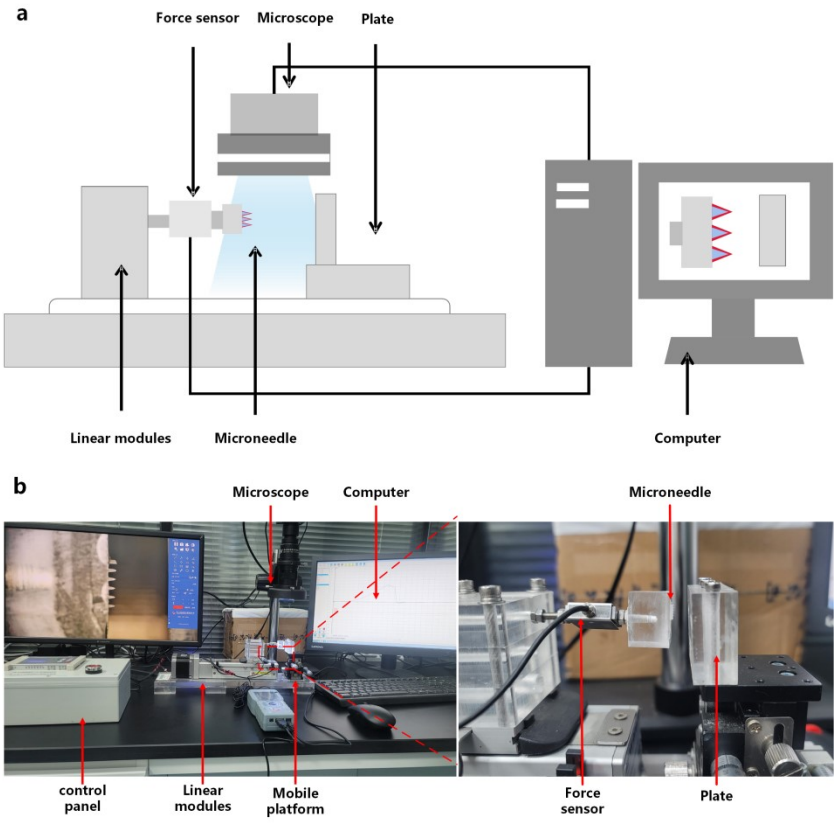

Fig. S3. (a) Schematic diagram of Mechanical properties testing machine. (b)Physical image of Mechanical properties testing machine.

S4. The calibration curve for DOX in PBS

First of all, 5 mg of doxycycline hydrochloride was added to 50 mL PBS solution, and stirred until completely dissolved, resulting in a stock solution with a concentration of 100 μg mL-1. Subsequently, 1.0, 2.0, 3.0, 4.0, and 5.0 mL of the stock solution were precisely added into separate 10 mL volumetric flasks, and PBS was added to each flask until the volume reached the 10 mL mark, resulting in a series of gradient solutions with concentrations of 10, 20, 30, 40, and 50 μg mL-1. Then, the absorbance of a series of standard DOX solutions were measured using a UV spectrophotometer (UV-3600 Plus, SHIMADZU, China). Finally, the absorbance values of each standard DOX solution at 274 nm were recorded, and and a calibration curve was established for gradient-diluted DOX, as shown in Fig. S4. The linear regression equation is as follows:

$y = 0.3141x + 0.00786$; $R^2 = 0.99977$

In the formula, y represents absorbance and x represents concentration.

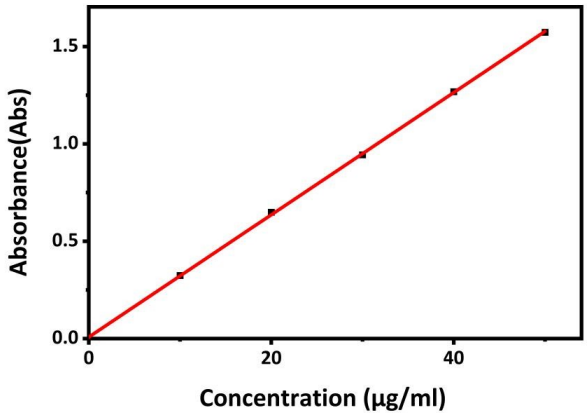

Fig. S4. The calibration curve for DOX in PBS

S5. The calibration curve for VEGF in Coomassie Brilliant Blue solution

Preparation of Coomassie Brilliant Blue Solution: First of all, 20 mg of Coomassie Brilliant Blue G-250 powder was added to 10 mL of 98% ethanol, and stirred until completely dissolved. Then add the mixed solution to 20mL of 85% phosphoric acid and dilute to 200mL with deionized water.

Preparation of Standard Solutions: 10 μg of VEGF was added to 100 μL of PBS solution, and stirred until completely dissolved, resulting in a stock solution with a concentration of 0.1 μg μL-1. Subsequently, 10, 20, 30, and 40 of the stock solution were precisely added into separate 1 mL Coomassie Brilliant Blue solution, resulting in a series of gradient solutions with concentrations of 1, 2, 3, and 4 μg mL-1.

Then, the absorbance of a series of standard VEGF solutions were measured using a UV spectrophotometer. Finally, the absorbance values of each standard VEGF solution at 645 nm were recorded, and and a calibration curve was established for gradient-diluted VEGF, as shown in Fig. S5. The linear regression equation is as follows:

$y = 0.0177x + 0.533$; $R^2 = 0.974$

In the formula, y represents absorbance and x represents concentration.

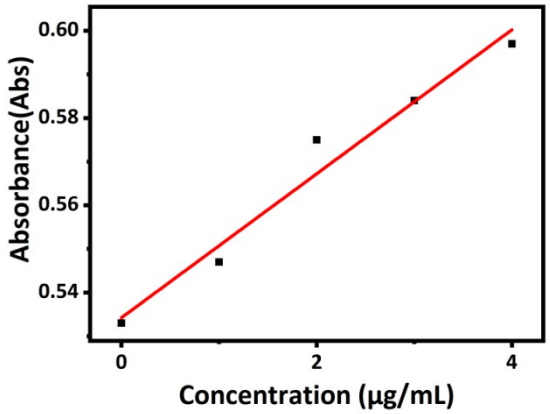

Fig. S5. The calibration curve for VEGF in Coomassie Brilliant Blue solution

S6. Evaluation on antimicrobial properties

The antibacterial activity of the CS/HA-bilayer MNs was evaluated using Gram-positive *S. aureus* (ATCC 6538) and Gram-negative *E. coli* (ATCC 25922) as bacterial models. Microneedle samples and 10 μL of bacterial suspension were added to 1 mL of PBS solution to obtain a mixed solution. Subsequently, 50 μL of the mixed solution was inoculated onto LB agar plates and incubated at 35° C for 3 days. The results, as shown in Fig. S6, indicate that the CS solution exhibits strong bactericidal activity against *S. aureus* and is less effective against *E. coli*. Additionally, only a few bacterial colonies were observed in the CS MNs group, while no bacterial growth was detected in the CS/HA-bilayer MNs group. These findings suggest that the CS/HA-bilayer MNs possess stronger antibacterial properties than the CS MNs. They effectively sterilize and inhibit bacterial growth, demonstrating excellent antibacterial activity against Gram-negative and Gram-positive bacteria.

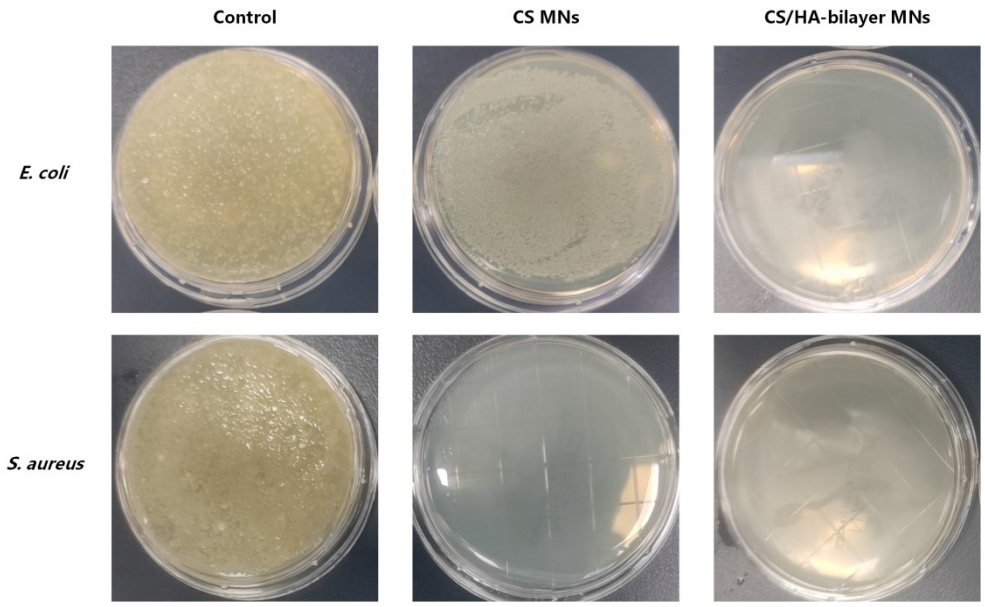

Fig. S6. The antibacterial effect of CS/HA-bilayer MNs against *E. coli* and *S. aureus*.

S7. Skin puncture test and skin healing test in vivo

In order to verify the biological safety of CS/HA-Bilayer MNs, mice were selected for skin puncture experiment. First, the back of the mice was depilated after anesthesia. Then, put the micro needle into the depilation area, press it for 1 minute and take out the micro needle. Then, the micro needling site was photographed at 0, 2, 5, and 10 minutes respectively through the optical microscope to observe the recovery and irritation of the skin. Finally, the skin of the puncture site was removed with surgical scissors, and 4% formaldehyde fixative was put into it for h&e staining.

As shown in Fig. S7 (a), clearly visible array holes are formed on the mouse skin, indicating that the microneedles have successfully penetrated the skin and have a good penetration rate. Due to the self-healing of rat skin, it can be seen that nearly half of the array holes have been completely contracted to close at the second minute. From the fifth minute to the tenth minute, it can be seen that the array holes caused by the microneedles have been basically closed. At this time, the array holes caused by the microneedles have been basically invisible. Therefore, it can be judged that the wound caused by micro acupuncture into the skin is very small, the skin can heal in a short time, and no obvious skin irritation symptoms are observed, as shown in Fig. S7 (b) for the results of micro needling into the skin section. After the flexible base micro needle array penetrates into the skin, it penetrates the cuticle of the skin and penetrates into the skin epidermis, leaving tiny wounds on the skin epidermis, of which the depth of the wounds is generally greater than 100um.

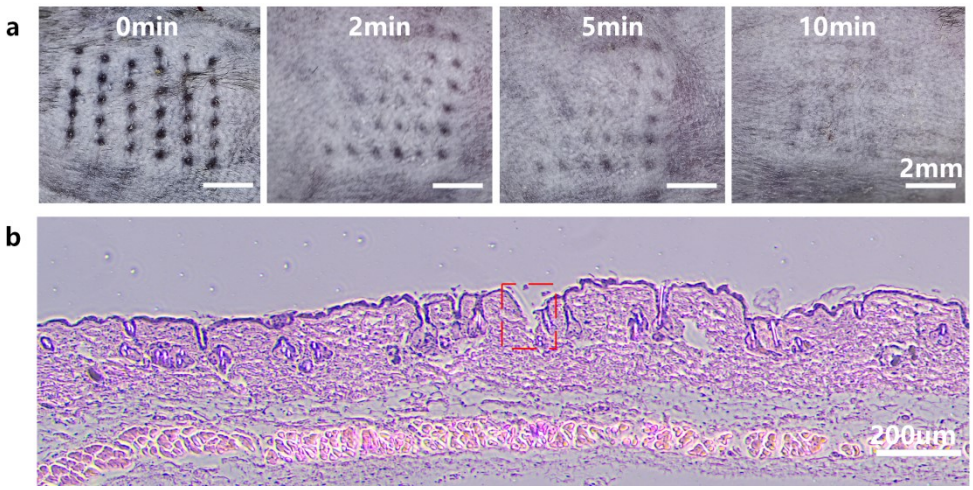

Fig. S7. (a)Optical images of mouse skin at 0, 2, 5, and 10 minutes after microneedle puncture. (b) H&E staining of skin tissue.

S8. The bacterial biofilm model in the wound

In this paper, a diabetic mice model was used to make an 8 mm-diameter wound on its back and inoculated with 50 μL of a bacterial suspension containing a mixture of E. coli and S. aureus to simulate a chronic infection environment. After two days of wound culture, dense and thick bacterial biofilm formation was observed, accompanied by a small amount of pus, indicating that the bacterial biofilm model had been successfully established in the wound of living mice before microneedle treatment, as shown in Fig. S8.

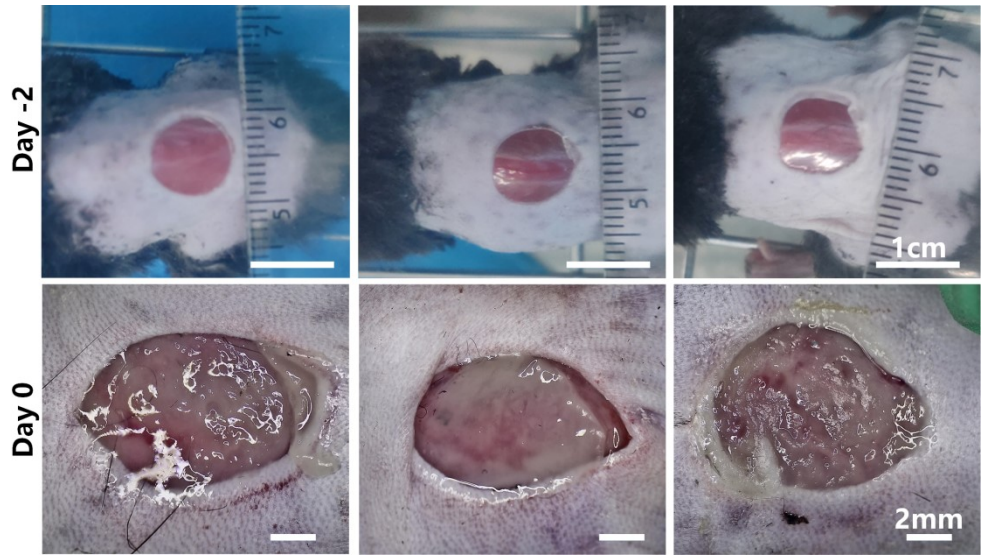

Fig. S8. Cultivation of *E. coli* and *S. aureus* on mouse wounds